High-Frequency Centimeter-Accuracy Water Level Estimation in the Yangtze River Using Multi-GNSS Interferometric Reflectometry

Shuanggen Jin, *Senior Member, IEEE*, Zilong Chen, and Hui Peng, *Member, IEEE*

***Abstract*—Water level measurement is essential for managing and conserving water resources. The Yangtze River has a significant impact on agriculture, transportation, and local ecosystems, while traditional water level measurement still has some limitations, e.g., high cost and low coverage. Recently, global navigation satellite system-interferometric reflectometry (GNSS-IR) has become a new means for water level monitoring. This article integrates the reflected signals from GPS, GLONASS, Galileo, and BDS constellations for real-time high-frequency water level estimation at Yangtze River stations (BADO and DATO). By integrating a sliding window with variational mode decomposition (VMD), iteratively reweighted least-squares (IRLS), and Savitzky–Golay (S–G) filtering, water level measurements at a 5-min temporal resolution are obtained and evaluated. Our individual and combined results show that the VMD method efficiently provides more accurate and stable inversion results using signal-to-noise ratio (SNR) data in each window. The combined and filtered results improved the accuracy by over 45.88% when compared to single-system measurements. The root-mean-square error (RMSE) was 4.86 cm at BADO and 2.28 cm at DATO with coefficient of determination (R^2) 0.99 at both stations. Our results demonstrated that the combined method enabled precise and continuous water level monitoring, which provides new pathways for hydrological monitoring and real-time water resource management.**

***Index Terms*—Global navigation satellite system-interferometric reflectometry (GNSS-IR), signal-to-noise ratio (SNR), variational mode decomposition (VMD), water level monitoring, Yangtze River.**

I. Introduction

WATER level data are a crucial basis for managing inland water resources, especially in flood-prone and drought-affected regions, where it plays a key role in disaster early warning systems. The Yangtze River, the third longest river in the world, carries an immense volume of water and experiences significant seasonal fluctuations. Monitoring the water levels of the Yangtze River is therefore crucial for managing flood risks, ensuring the safety of millions of people living in its basin, and supporting water resource management for agriculture, industry, and ecological protection. However, traditional water gauges for monitoring water levels are labor-intensive and prone to errors from vertical crustal deformations at hydrological stations. Satellite altimetry technology has high spatial resolution, but the sampling rate is low. In addition, due to the complex terrain in coastal areas, the radar beam may receive echoes from both the ocean and the land when it is close to the coastline, resulting in inaccurate altitude measurements [1]. Consequently, an alternative solution is required with reliable performance in all-weather conditions and high spatial–temporal sampling.

The global navigation satellite system (GNSS) provides all-weather, around-the-clock, high-precision positioning, navigation, and timing (PNT) services [2]. Hall and Cordey [3] firstly introduced the concept of GNSS-based reflectometry. Over the following decades, GNSS reflectometry has been extensively studied and proven effective for various applications, including ocean altimetry [4], typhoon monitoring [5], sea ice detection [6], soil moisture retrieval [7], and snow depth estimation [8]. Martin-Neira [9] proposed the use of delays between direct and reflected GPS signals for altimetry known as the passive reflectometry and interferometry system (PAIRS). Anderson [10] later introduced the widely used signal-to-noise ratio (SNR) method, namely GNSS-interferometric reflectometry (GNSS-IR). SNR data can be collected from just a single GPS antenna [11], offering simplicity and cost efficiency when compared to phase delay methods [12]. Larson et al. [13] used SNR data from conventional geodetic GPS receivers to retrieve coastal sea level variations and later introduced a dynamic sea surface model with adjusted heights by incorporating sea level change rates [14]. Other researchers have demonstrated the feasibility of using additional GNSS systems for water level retrieval, such as GLONASS [15] and BDS [16]. Roussel et al. [17] tested the performance of combined GPS and GLONASS retrievals and calculated both sea level and rate of change using the least-squares method (LSM) with achieving a correlation coefficient of over 0.97. Wang et al. [18] proposed a robust regression approach using a sliding window from combining multi-GNSS constellations and obtained 10-min interval water

Received 24 February 2025; revised 8 May 2025 and 9 June 2025; accepted 16 July 2025. Date of publication 30 July 2025; date of current version 7 August 2025. This work was supported in part by Henan International Science and Technology Cooperation Key Program under Grant 241111520700 and in part by the Tianjin Key Research and Development Program under Grand 24YFYSHZ00110. *(Corresponding author: Shuanggen Jin.)*

Shuanggen Jin is with the School of Surveying and Land Information Engineering, Henan Polytechnic University, Jiaozuo 454003, China, also with the School of Remote Sensing and Geomatics Engineering, Nanjing University of Information Science and Technology, Nanjing 210044, China, and also with the School of Artificial Intelligence, Anhui University, Hefei 230601, China (e-mail: sgjin@hpu.edu.cn).

Zilong Chen and Hui Peng are with the School of Remote Sensing and Geomatics Engineering, Nanjing University of Information Science and Technology, Nanjing 210044, China.

Digital Object Identifier 10.1109/TGRS.2025.3594071

level with accuracy improved by approximately 40%–75%. Strandberg et al. [19] introduced an inverse model for sea surface altimetry with parameterizing the smoothed sea surface using B-spline curves, and simultaneously estimated the inverse model coefficients and sea surface B-spline parameters as well as sea surface retrieval using SNR observations as input for least-squares calculations. He later incorporated Kalman filtering to demonstrate the feasibility of real-time sea surface altimetry [20].

SNR signals typically contain direct signals, reflected signals, and noise. When using GNSS-IR technology for altimetry, it is essential to accurately extract the reflected signal by removing the direct signal component, a process known as detrending. This is commonly done by fitting the direct signal component with a low-order polynomial and then subtracting it [13]. To enhance the utility of SNR data and improve the accuracy of spectral analysis, Beckheinrich et al. [21] proposed using empirical mode decomposition (EMD) for detrending SNR data. However, in practice, the EMD method often suffers from mode mixing, which reduces the accuracy and reliability of the decomposition results. To address this issue, Lee et al. [22] tested the ensemble empirical mode decomposition (EEMD) method and evaluated its effectiveness in handling the trend component. Other researchers have tested the effectiveness of singular spectrum analysis (SSA) in extracting interference frequencies [23], [24]. Hu et al. [25] applied the variational mode decomposition (VMD) method to decompose SNR data and remove the trend component. The results showed that this method offered higher accuracy and stability when compared to other approaches. However, temporal resolution and accuracy are still low.

To balance both temporal resolution and accuracy, in this article we proposed a combined approach with integrating a sliding window, VMD, iterative reweighted least-squares (IRLS), and Savitzky–Golay (S–G) filtering. Using this combined approach, a high temporal resolution with centimeter-level accuracy for water level monitoring is conducted along the Yangtze River mainstream. Section II introduces the GNSS-IR inversion model and the detailed method as well as GNSS observation at the Yangtze River sites (BADO and DATO). Section III presents the performance of water level estimation from both single-system and multi-system approaches. Section IV provides a discussion of the results. Finally, conclusion is given in Section V.

II. Methods and Data

A. GNSS-IR Altimetry Model

The basic GNSS-IR model for water surface height retrieval is illustrated in Fig. 1. The GNSS antenna simultaneously receives both direct and reflected signals, and their interference effect is captured in the SNR data.

The SNR of ground-based reflection can be expressed as follows [27]:

$$\mathrm{SNR} = \frac{P_s}{P_n} = \left(P_d + P_r + P_r^i + 2\sqrt{P_d P_r}\cos\left(\Psi + \phi\right)\right) P_n^{-1} \tag{1}$$

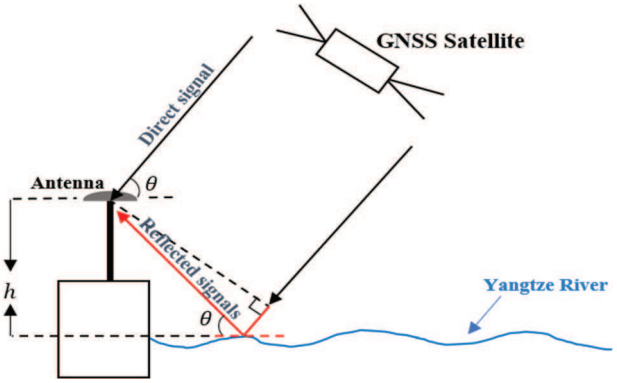

Fig. 1. Geometric paths of GNSS direct and reflected signals [26].

where P_s is the received signal power; P_n is the noise power; P_d and P_r represent the power of the direct and reflected signals, respectively; P_r^i is the incoherent power; Ψ is the phase delay between the direct and reflected signals; and ϕ is the additional phase shift introduced by reflection (e.g., random phase variations caused by surface roughness). The SNR can typically be decomposed into a trend term tSNR and an oscillatory term δSNR

$$t\mathrm{SNR} = \left(P_d + P_r + P_r^i\right) P_n^{-1} \tag{2}$$

$$\delta\mathrm{SNR} = 2\sqrt{P_d P_r} P_n^{-1} \cos\left(\Psi + \phi\right). \tag{3}$$

Due to the significant path attenuation of GNSS reflected signals and the directional design of the receiving antenna (which suppresses low-elevation gain), $P_d \gg P_r$, and P_r^i is a slowly varying specular component. Thus, tSNR is primarily dominated by P_d. By detrending the original SNR time series, the high-frequency oscillatory component δSNR can be extracted. This oscillatory term contains information about the geometric path difference and is directly related to the height of the reflecting surface.

Assuming that the water surface is still and a specular reflection occurs, the difference between the reflected and direct paths is $D = 2h\sin\theta$, and the phase delay Ψ is expressed as follows [28]:

$$\Psi = \frac{2\pi D}{\lambda} = \frac{4\pi h \sin\theta}{\lambda} \tag{4}$$

where h represents the height of the antenna above the water surface, θ is the elevation angle between the satellite and the antenna, and λ is the carrier wavelength. δSNR can be expressed as

$$\delta\mathrm{SNR} = A\cos\left(\frac{4\pi h}{\lambda}\sin\theta + \phi\right) \tag{5}$$

where A represents the amplitude. The frequency f of the SNR arc is expressed as

$$2\pi f = \frac{d\Psi}{d\sin\theta} = \frac{4\pi \bar{h}}{\lambda}. \tag{6}$$

Due to the uneven sampling of elevation angles, the frequency is extracted using the Lomb–Scargle periodogram (LSP) [29], [30], [31], allowing the determination of the water surface elevation $\bar{h}$. Since the water surface is dynamic, the

TABLE I
CORRELATION COEFFICIENTS AND KURTOSIS OF THE MAXIMUM CORRELATION COEFFICIENT OF IMF COMPONENTS FOR SNR DATA FROM BADO AND DATO AT DIFFERENT K VALUES

	BADO			DATO		
K	2	3	4	2	3	4
IMF1	0.7956	0.1370	0.1193	0.9012	0.1735	0.0667
IMF2	0.6685	0.7950	0.1257	0.4745	0.8937	0.1779
IMF3	/	0.6646	0.7944	/	0.4673	0.8929
IMF4	/	/	0.6624	/	/	0.4665
Kurtosis	2.3899	2.3851	2.3822	1.6535	1.6335	1.6308

static assumption introduces estimation errors. By introducing the rate of change in height $\dot{h} = (dh/dt)$ to model the dynamic water surface, (6) is rewritten as follows [17]:

$$2\pi f = \frac{4\pi}{\lambda}\left(\frac{\tan\theta}{\dot{\theta}}\dot{h} + h\right) \tag{7}$$

where $\dot{\theta}$ represents the rate of change of the elevation angle. According to (6) and (7), we obtain

$$\bar{h} = \frac{\lambda f}{2} = \frac{\tan\theta}{\dot{\theta}}\dot{h} + h. \tag{8}$$

B. Sliding Window for SNR Time Series

Previous studies have frequently used sliding windows to enhance retrieval performance and temporal resolution [32]. The choice of sliding window length is crucial [17]. The window length cannot be too large. If the observable orbit of a single satellite spans several hours, significant deviations in the retrieval results may occur due to variations in oscillation frequency. Conversely, the window length should not be too short, and it must provide enough data to accurately determine the frequency f through the LSP method. The choice of sliding window interval is also important, as it directly affects the temporal resolution of the output. In this study, a 40-min sliding window length and a 5-min interval were chosen, and the SNR time series was divided into equal segments. In addition, some satellite SNR arcs within the window include both ascending and descending arcs, which may lead to estimation errors [13]. Therefore, we excluded these arcs from the window to improve retrieval accuracy. Finally, we applied the VMD method to SNR time series exceeding 300 s within the window and then converted them to static reflection elevation $\bar{h}$ through the LSP method. To ensure the reliability of results, quality control of the static reflection height $\bar{h}$ is performed, and results with peak amplitudes less than 7 and peak noise ratios (PNRs) less than 3 are discarded. Within the window, outliers are removed based on the interquartile range [32], and the height h is jointly estimated using the IRLS method.

C. Variational Mode Decomposition

Hu et al. [25] proposed a GNSS-IR sea level height estimation model based on the VMD method. VMD can decompose SNR data into residual sequences and intrinsic mode functions (IMFs) that represent different local features. By analyzing these IMFs, the component representing the trend in the SNR data can be identified. The remaining IMFs are then reconstructed to extract the oscillatory component of the SNR data. Finally, the oscillation frequency is extracted from the SNR sequence using the LSP method to determine the sea level height. This method is more robust with respect to signal sampling and noise [33]. Fig. 2 compares the results of the VMD method with quadratic fitting (QF). The VMD method effectively distinguishes noise and useful components in the signal with improving the utilization of SNR data.

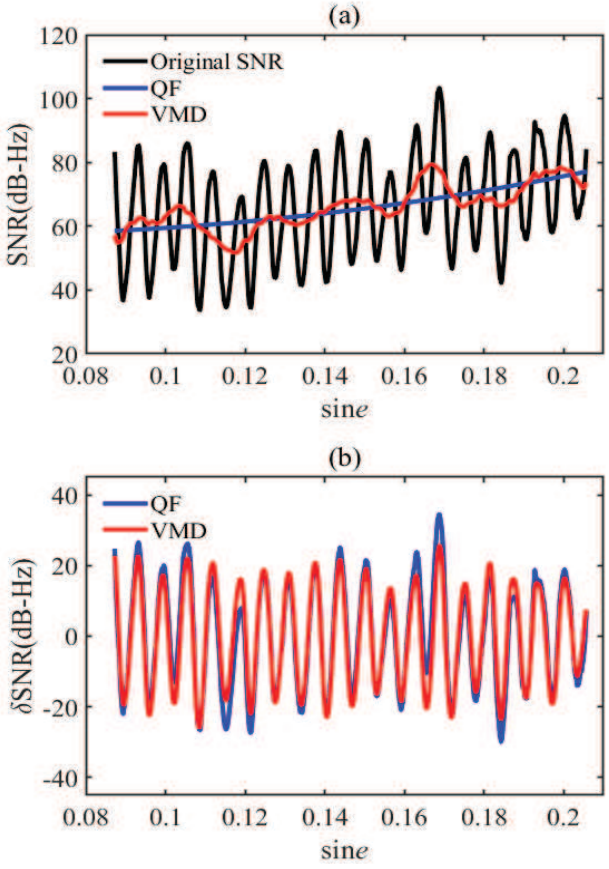

Fig. 2. (a) Effectiveness of QF and VMD in fitting direct signal components compared to original SNR. (b) Effectiveness of QF and VMD in extracting **δSNR**.

The fundamental idea of VMD is to decompose a signal into several amplitude- and frequency-modulated signals, which are a set of mode functions with different central frequencies and narrowband characteristics. The kth mode function $u_k(t)$ can

be expressed as

$$u_k(t) = A_k(t)\cos(\varphi_k(t)) \tag{9}$$

where $A_k(t)$ is the instantaneous amplitude and $\varphi_k(t)$ is the instantaneous phase. The original SNR time series $N(t)$, after VMD decomposition, can be represented as

$$N(t) = \sum_{k=1}^{K} u_k(t) + r(t) \tag{10}$$

where $r(t)$ is the residual term. The IMFs in VMD are defined as amplitude- and frequency-modulated signals. By optimizing the variational model, the optimal mode functions $u_k(t)$ and central frequencies ω_k are found such that the sum of the bandwidths of each mode function is minimized. Theoretically, the constrained variational is expressed as

$$\min_{\{u_k\},\{w_k\}} \left\{ \sum_{k=1}^{K} \left\| \partial_t \left[\left(\delta(t) + \frac{j}{\pi t} \right) * u_k(t) \right] e^{-j\omega_k t} \right\|_2^2 \right\} \tag{11}$$

$$\text{s.t.} \sum_{k=1}^{K} u_k = N(t) \tag{12}$$

where $\{u_k\}$ and $\{\omega_k\}$ denote the sets of mode functions and central frequencies, respectively. $[(\delta(t)+(j/\pi t))*u_k(t)]$ represents the Hilbert transform of the analytic signal. $e^{-j\omega_k t}$ represents the modulation operation used to shift the mode function $u_k(t)$ from the baseband to the central frequency ω_k, where j is the imaginary unit. To solve the optimal solution to the constrained variational problem, VMD introduces Lagrange multipliers and a quadratic penalty factor, transforming the constrained variational problem into an unconstrained one. The augmented Lagrange expression is

$$\begin{aligned} &\mathcal{L}(\{u_k\},\{\omega_k\},\lambda) \\ &= \alpha \sum_{k=1}^{K} \left\| \partial_t \left[\left(\delta(t) + \frac{j}{\pi t} \right) * u_k(t) \right] e^{-j\omega_k t} \right\|_2^2 \\ &\quad + \left\| N(t) - \sum_{k=1}^{K} u_k(t) \right\|_2^2 + \left\langle \lambda(t), N(t) - \sum_{k=1}^{K} u_k(t) \right\rangle \end{aligned} \tag{13}$$

where α is the penalty parameter and $\lambda(t)$ is the Lagrange multiplier. Before satisfying the stopping criteria for iteration, VMD alternately updates the mode functions u_k and central frequencies ω_k using the alternating direction method of multiplier (ADMM) until convergence. Each mode function is shifted from the baseband back to its original frequency band, resulting in K IMF components from the mode decomposition. The number of IMF components determines the level of detail in the decomposition results. Choosing an appropriate value for K helps in more accurate interpretation and analysis of the signal. To determine the optimal number of decomposition layers [34], the kurtosis of the IMF component with the highest correlation coefficient to the original SNR signal is calculated for different values of K. Table I shows the correlation coefficients of IMF components for SNR data from DATO and BADO at different K values, along with the kurtosis of the maximum correlation coefficient. The final choice for the VMD decomposition value of K is 2.

D. Iteratively Reweighted LSM

To obtain high-frequency water level data for the Yangtze River, the SNR time series is segmented using a sliding time window, with a window length of 40 min and a 5-min interval. To ensure the accuracy of the inversion, quality control is applied to the results within each window. Subsequently, the height h is jointly estimated using the IRLS method.

Since $\dot{h}$ in (8) cannot be directly computed, Roussel et al. [17] proposed using a classical LSM to simultaneously estimate h and $\dot{h}$. Within the ith sliding window, the reflected surface height of the pth satellite and the qth signal, obtained through LSP time–frequency transformation, is denoted as $\bar{h}_{pq}$. A matrix equation incorporating multiple observations is constructed as follows:

$$\begin{pmatrix} \cdots \\ \bar{h}_{pq} \\ \cdots \end{pmatrix} = \begin{pmatrix} \cdots & \cdots \\ 1 & \frac{\tan(\theta_p)}{\dot{\theta}_p} + (t_{pq} - t_i) \\ \cdots & \cdots \end{pmatrix} \begin{pmatrix} h \\ \dot{h} \end{pmatrix} \tag{14}$$

where t_{pq} represents the central epoch of the qth signal from the pth satellite within the sliding window and t_i denotes the central epoch of the ith window. Simplifying (14) yields

$$L_{i_{(n\times 1)}} = B_{i_{(n\times 2)}} X_{i_{(2\times 1)}} \tag{15}$$

where $L_{i_{(n\times 1)}} = \begin{pmatrix} \cdots \\ \bar{h}_{pq} \\ \cdots \end{pmatrix}$, $B_{i_{(n\times 2)}} = \begin{pmatrix} \cdots & \cdots \\ 1 & (\tan(\theta_p)/\dot{\theta}_p) + (t_{pq} - t_i) \\ \cdots & \cdots \end{pmatrix}$, $X_{i_{(2\times 1)}} = \begin{pmatrix} h \\ \dot{h} \end{pmatrix}$, and n is the number of effective inversion results for each system within the window. Solving X_i using LSM provides the solution for the mth iteration within the ith window as follows:

$$X_i^{(m)} = \left(B_i^T P_i^{(m)} B_i \right)^{-1} B_i^T P_i L_i^{(m-1)} \tag{16}$$

where P represents the weight matrix. The PNR of LSP is an indicator of signal quality, with its magnitude reflecting the quality of the signal. Therefore, this study uses PNR values to set the initial weight matrix. Considering the varying precision of different signals [18] and the potential presence of large errors within the window, the IGG III weight function is employed to update the weight matrix and enhance the performance of the LSM [35]. The weight function is given as follows [36]:

$$V_i^{(m)} = B_i X_i^{(m)} - L_i^{(m-1)} \tag{17}$$

$$p_{ss}^{(m)} = \begin{cases} p_{jj}^{(m-1)} & \left|v_s^{(m)}\right| \le k_0 \\ \dfrac{p_{ss}^{(m-1)} k_0}{\left|v_s^{(m)}\right|} \left(\dfrac{k_1 - \left|v_s^{(m)}\right|}{k_1 - k_0} \right)^2 & k_0 < \left|v_s^{(m)}\right| \le k_1 \\ 0 & \left|v_s^{(m)}\right| > k_1 \end{cases} \tag{18}$$

where $V_i^{(m)}$ represents the residual vector from the mth iteration in the ith window, $p_{ss}^{(m)}$ denotes the sth row and the sth column element of the weight matrix, and k_0 and k_1 are constants. The standard residual of the sth element of the residual vector $v_s^{(m)} = V_s^{(m)} \Big/ (\sigma_0((1/p_{ss}^{(m-1)}) - B_{i_s}(B_i^T P^{(m-1)} B_i)^{-1} B_{i_s}^T)^{1/2})$. σ_0 is the unit weighted root-mean-square error (RMSE) given by

$[(V^{(m)})^T P^{(m-1)} V^{(m)}/n-2]^{1/2}$, and B_{i_s} denotes the sth row of B_i. The updated weight matrix is then used in (14) to solve X_i, with the iteration stopping when the change in X meets the following condition:

$$\left\| X^{(m+1)} - X^{(m)} \right\| < \xi. \tag{19}$$

E. S–G Filtering

The S–G filter smooths data by fitting a polynomial to a local data window using least-squares, then replacing the original data points with the values from this polynomial fit. The S–G filter outperforms other smoothing methods, such as moving averages, in preserving high-frequency components of the data, such as sharp peaks and abrupt changes [32]. The filtered results of the IRLS combination are processed by applying the S–G filter. In each filtering window (with a length of $2w+1$), while the water level h is fit with the r-degree polynomial

$$\tilde{h}_u = \sum_{j=0}^{r} c_j u^j \tag{20}$$

where $\tilde{h}_u$ represents the fit result, u ranges from $[-w, w]$, and c_j is the polynomial coefficients. The sum of squared residual E between the fit data points and the original data points is given by

$$E = \sum_{u=-w}^{w} \left(\tilde{h}_u - h_u\right)^2. \tag{21}$$

The polynomial coefficients c_j are determined using least-squares. To achieve the best fit, the goal is to minimize the sum of squared residuals E. This is done by taking the partial derivative of E with respect to the polynomial coefficients c_j and setting it to zero, leading to the final solution

$$\sum_{u=-w}^{w} h_u u^j = \sum_{j=0}^{r} c_j \sum_{u=-w}^{w} u^{j+z} \tag{22}$$

where z denotes the order of differentiation. Once a number of points on one side w, the polynomial degree r, and the data h_u to be fit are known, the polynomial can be determined. The fit polynomial is used to estimate the value at the center of the filtering window. For subsequent points, this process is repeated by continually moving the window.

The steps for estimating water level in the Yangtze River using the GNSS-IR combined algorithm are as follows.

1) Use a sliding time window to segment the original SNR time series into 40-min segments with a 5-min step.
2) Apply the VMD method to extract reflection signals from the SNR segments within the window and then use the LSP method to determine the reflection height.
3) Perform quality control on the retrieval results within the window.
4) Combine the reflection heights from all signals within the window using IRLS, and assign weights through the IGG III weighting matrix.
5) Apply S–G filtering to the combined reflection heights to obtain the final Yangtze River water level estimation with a 5-min interval.

TABLE II
BADO AND DATO OBSERVABLE DATA TYPES

	BADO	DATO
GPS	S1C、S2W、S5X	S1C、S2W、S5X
GLONASS	S1C、S2C	S1C、S2C
BDS	S1I、S7I	S1I、S6I、S7I
Galileo	S1X、S8X	S1X、S5X、S7X

F. GNSS Observation Data

Two continuous GNSS-IR water level monitoring stations were installed in the river's upper and lower reaches along the Yangtze River, named BADO and DATO. BADO is located within the Three Gorges Reservoir area, where operational scheduling causes frequent water level fluctuations with annual variations reaching 30 m. DATO, positioned at the final hydrological control station before the Yangtze River discharges into East China Sea, serves as a benchmark for downstream discharge measurements and basin-wide water resource evaluation. Its water level changes are essential for long-term hydrological monitoring and flood forecasting. These sites represent two distinct hydrological regimes: a highly dynamic upstream region and a discharge downstream region in the Yangtze River. Together, they form an experimental platform for assessing the generalizability and robustness of the proposed GNSS-IR combined method.

BADO is equipped with a CHCNAV N72 receiver and an A230RGB antenna, while DATO has a CHCNAV P5 receiver and an A230RGB antenna. Both GNSS-IR stations were installed directly within the national hydrological stations, with their receivers positioned approximately 10–30 m from the river surface. These stations collect multi-GNSS observational data at a 1-Hz sampling rate (observable types are listed in Table II). The data from both stations are transmitted in real time to the Huawei cloud server via a data transfer unit (DTU). Users can access the cloud server through file transfer protocol (FTP) to download and process the observational data locally.

To validate the accuracy of GNSS-IR water level retrieval, in situ measurements from hydrological stations collocated with the BADO and DATO GNSS sites were used as reference. These hydrological stations are equipped with WFX-40 float-type water level gauges for continuous high-frequency monitoring (sampling interval of 5 min), and RD-300C radar water level gauges as backup instruments under abnormal conditions. The reference water level data used in this study were authorized and provided by the Ministry of Water Resources of China, serving as a reliable benchmark for evaluating the accuracy of GNSS-IR results.

Fig. 3(a) shows the geographical locations of the BADO and DATO sites, while Fig. 3(b) and (d) illustrates the installed antennas and the surrounding environment. The MATLAB toolbox [38] was used to plot the first Fresnel zone at different elevation angles for the BADO and DATO sites [Fig. 3(c) and (e)]. To ensure that the receiver's reflected signals originate from the river surface, the final selected

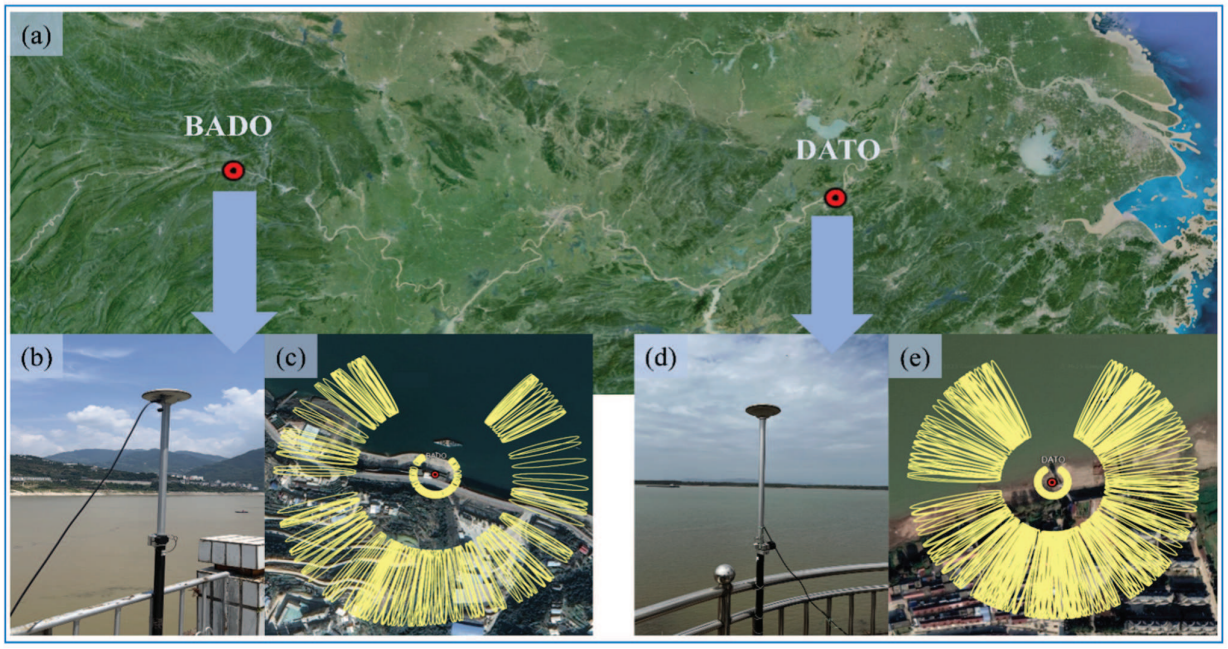

Fig. 3. (a) Geographic locations of BADO and DATO. (b) and (d) Antennas and surrounding environments at BADO and DATO stations, respectively. (c) First Fresnel zone at BADO station for elevation angles of 5° and 25°. (e) First Fresnel zone at DATO station for elevation angles of 5° and 30°.

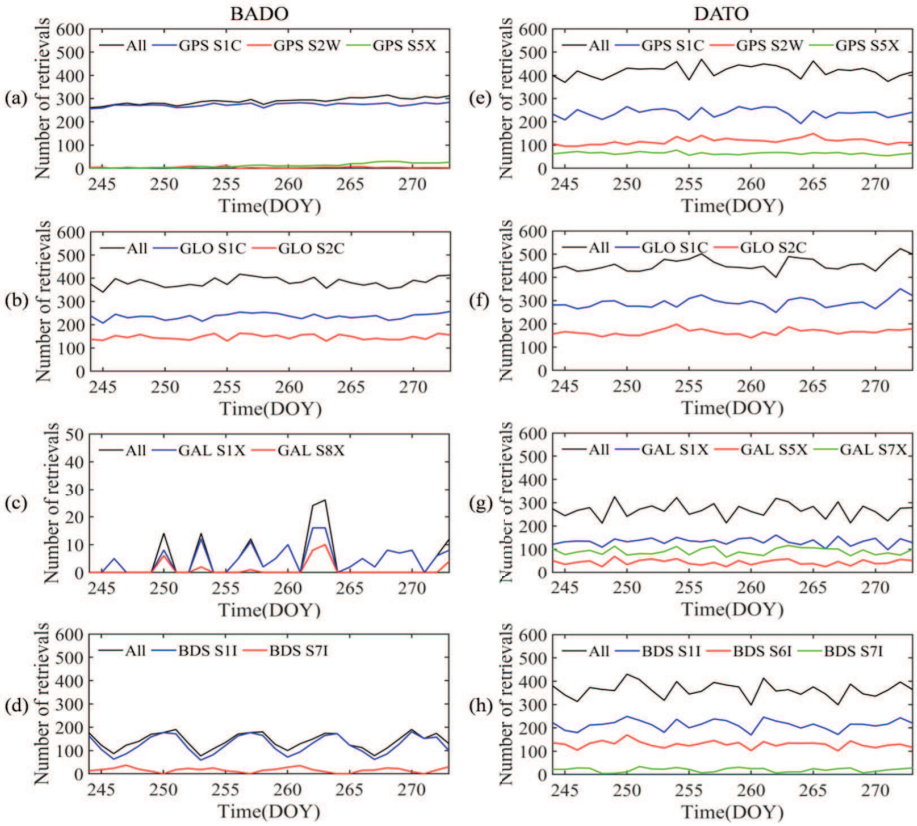

Fig. 4. Number of valid daily retrievals for each signal type at BADO: (a) GPS, (b) GLONASS, (c) Galileo, and (d) BDS; and DATO: (e) GPS, (f) GLONASS, (g) Galileo, and (h) BDS.

elevation and azimuth angles were set as follows: BADO with an elevation range of [5°, 25°] and azimuth ranges of [0°, 100°] and [300°, 360°]; DATO with an elevation range of [5°, 30°] and azimuth ranges of [0°, 70°] and [250°, 360°]. This study uses SNR data collected from BADO and DATO in September 2023 (DOY 244–273) to evaluate the performance of the combined algorithm and its application in inland rivers.

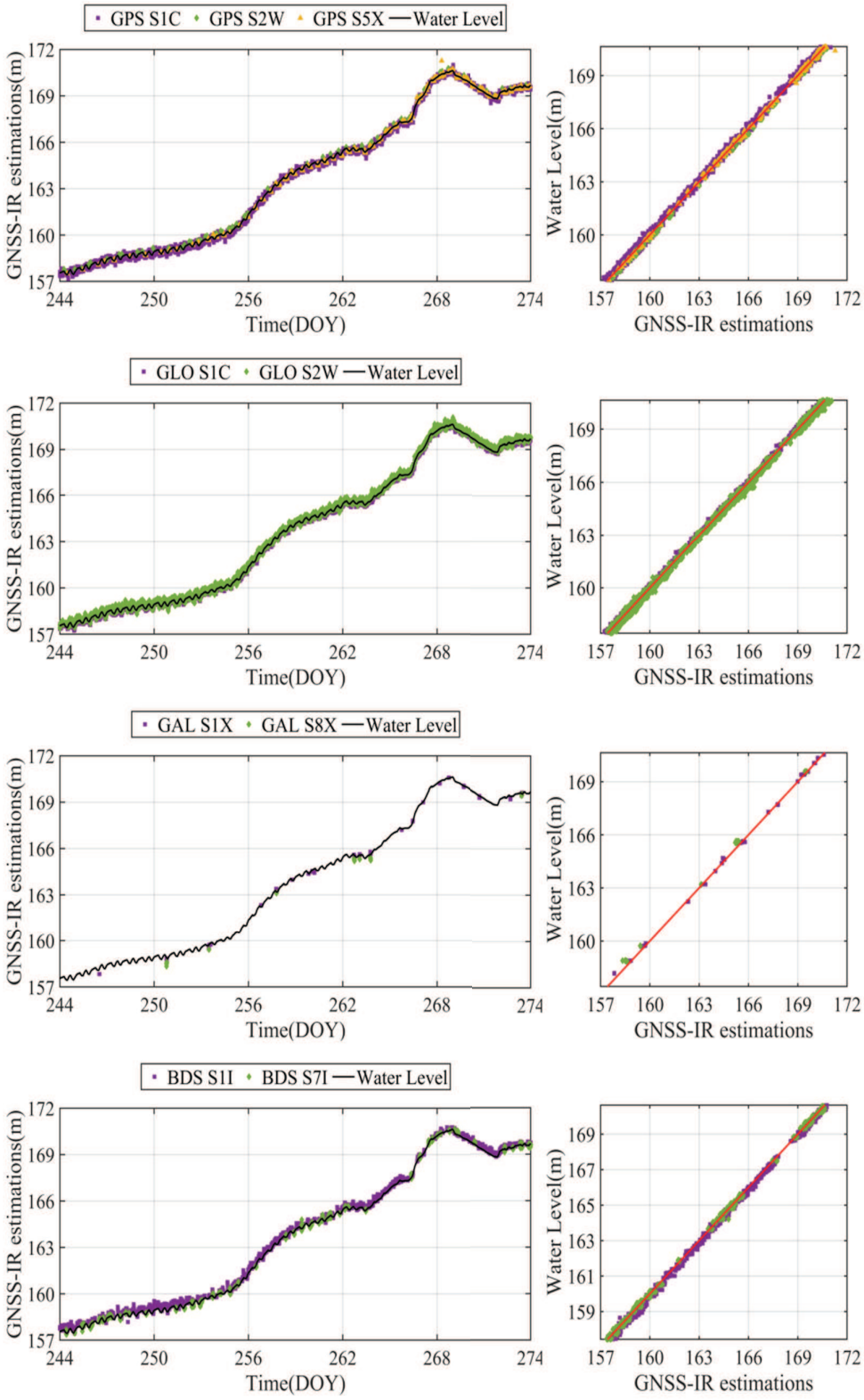

Fig. 5. Water level results and correlation analysis for each system at BADO station.

III. Results and Analysis

A. Performance of Single GNSS-IR

To assess the performance of various signals within the sliding window, we applied the VMD and LSP methods to retrieve reflection heights for each SNR type (see steps 1–3 in Section II). Fig. 4 shows the daily number of retrievals for each frequency band at the two stations (BADO and DATO) during DOY 245–270. The daily average number of retrievals at both sites is ranked as: GLONASS > GPS > BDS > Galileo.

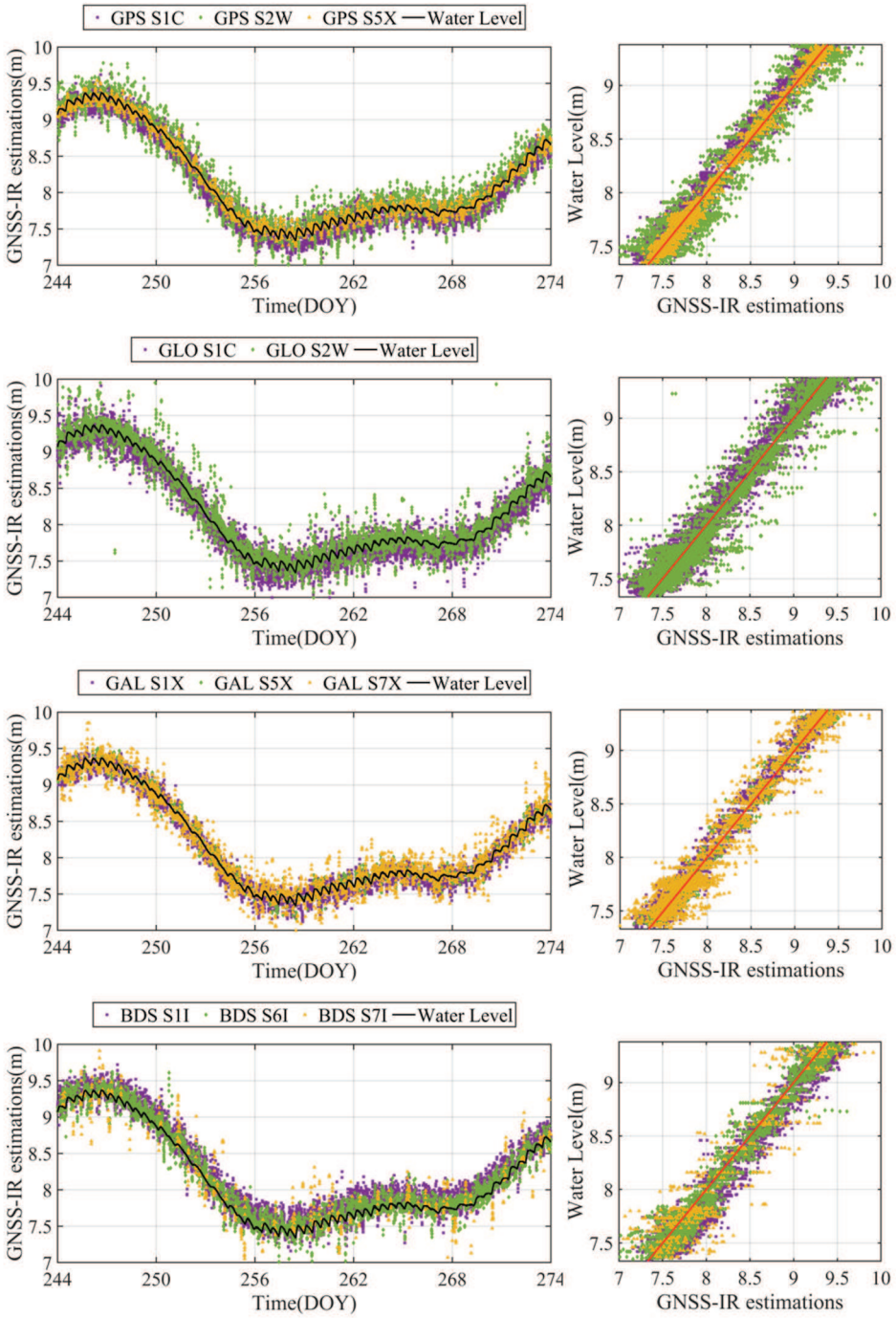

Fig. 6. Water level results and correlation analysis for each system at DATO station.

Figs. 5 and 6 show the time series of water surface heights retrieved for each SNR type at both sites, along with a correlation analysis when compared to water gauge measurements. To evaluate the performance of each signal, Table III provides the RMSE and R^2 values of the water surface height retrievals for each SNR type.

For the GPS system, the total number of retrievals at BADO remained relatively stable throughout the whole period, ranging from approximately 200–300. The S5X band exhibited the highest accuracy but had a daily retrieval count of only 12. The S1C band had the highest number of retrievals among GPS bands, with an average of 273 results per day. At DATO, the retrievals remained consistent at around 400 per day, with the S1C band contributing 238 and S2W about 116. The S5X band demonstrated the highest accuracy, with an RMSE of 7.01 cm. The GLONASS system provided the highest daily retrievals at both stations, with the S1C band showing the best accuracy and highest contribution. At BADO, the RMSE for GLONASS-S1C was 8.98 cm. The scatter plot of GLONASS retrieval results at DATO shows a high correlation (Fig. 6), although it is slightly larger when compared to GPS scatter, indicating that GLONASS signals might have slightly higher

TABLE III
DAILY AVERAGE RETRIEVAL COUNTS, RMSE, AND CORRELATION COEFFICIENT FOR EACH SNR TYPE AT BADO AND DATO

Observation Code	BADO			DATO		
	Number	RMSE (cm)	R	Number	RMSE (cm)	R
GPS-S1C	8195	11.56	0.99	7128	11.07	0.99
GPS-S2W	117	18.61	0.99	3485	17.00	0.96
GPS-S5X	366	9.56	0.99	1930	7.01	0.99
GLONASS-S1C	7088	8.98	0.99	8726	13.84	0.98
GLONASS-S2C	4402	16.40	0.99	4946	17.52	0.96
Galileo-S1X	136	12.26	0.99	3995	10.40	0.99
Galileo-S5X	/	/	/	1318	8.97	0.99
Galileo-S7X	/	/	/	2729	14.92	0.97
Galileo-S8X	31	27.83	0.99	/	/	/
BDS-S1I	3752	18.22	0.99	6412	13.83	0.98
BDS-S6I	/	/	/	3889	12.21	0.98
BDS-S7I	485	11.77	0.99	594	27.07	0.91

TABLE IV
COMPARISON OF THE RESULTS OF QF, EMD, SSA, AND VMD MULTISYSTEM COMBINATION

	BADO			DATO		
	RMSE(cm)	R^2	Number	RMSE(cm)	R^2	Number
QF	13.13	0.99	8021	10.20	0.98	8502
EMD	8.39	0.99	7957	6.55	0.99	8376
SSA	8.38	0.99	7920	6.39	0.99	8474
VMD	7.90	0.99	8057	5.99	0.99	8475

noise levels or variability. For the Galileo system, the number of retrievals at the BADO station was low, ranging from 0 to 30, with 12 days showing no retrievals. The average daily retrievals for the S1X and S8X bands were approximately 5 and 1, respectively. At DATO, the average daily retrievals were approximately 268. The S5X band had the highest accuracy, with an RMSE of 8.97 cm, despite having the fewest retrievals. For the BDS system, both stations achieved decimeter-level observation accuracy. BADO had an average of about 141 retrievals per day, with the S1I band contributing the most, approximately 125, and S7I contributing about 16. DATO had an average of about 363 retrievals per day, with the main contribution from S1I, followed by S6I and S7I.

The results demonstrate that the performance of the GNSS-IR method varies across different satellite systems and frequency bands. At both BADO and DATO, the GPS and GLONASS systems produced a high number of stable retrievals, indicating consistent signal quality and reliable water level data. Most bands in both datasets showed low RMSE values and high correlation, indicating that the VMD method offers high accuracy and stability. However, certain bands, such as GLONASS-S1C and BDS-S7I, exhibited notable variations between the datasets, warranting further analysis of their stability and reliability. The DATO site had a higher number of retrievals for the Galileo and BDS systems compared to BADO, possibly due to differences in the receivers used at the stations. The increased number of retrievals for each system at DATO indicates that GNSS-IR has more and more data sources, which will effectively improve the temporal resolution of GNSS-IR water level inversion.

B. Performance of Multi-GNSS Combination

In this section, we processed the SNR data within each window using four methods: QF, EMD, SSA, and VMD. We then analyzed these processed signals using the LSP method and combined the results from multiple GNSS systems using IRLS. We compared the combined water level retrieval results obtained from these four methods. Table IV presents the statistics of the 5-min water level results from DOY 244–274 for each method. At both BADO and DATO stations, the RMSE for the VMD method was 7.9 and 5.99 cm, outperforming the other three methods and showing a 40% and 41% improvement in accuracy when compared to QF. The accuracy of the EMD and SSA methods is comparable, outperforming the QF method. The total number of valid retrievals using VMD was 8057 and 8475, slightly higher than other methods (with DATO station's VMD slightly lower than QF). These

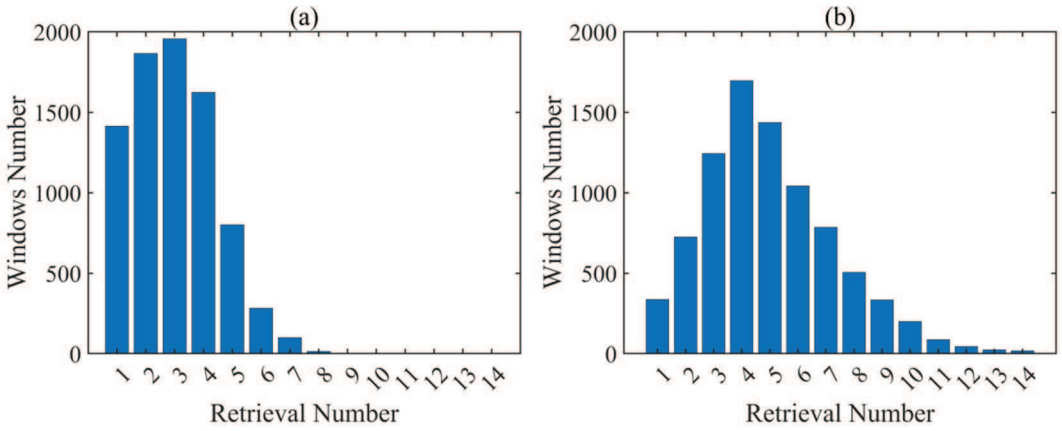

Fig. 7. Valid retrieval number and corresponding window counts for the combination algorithm at (a) BADO and (b) DATO.

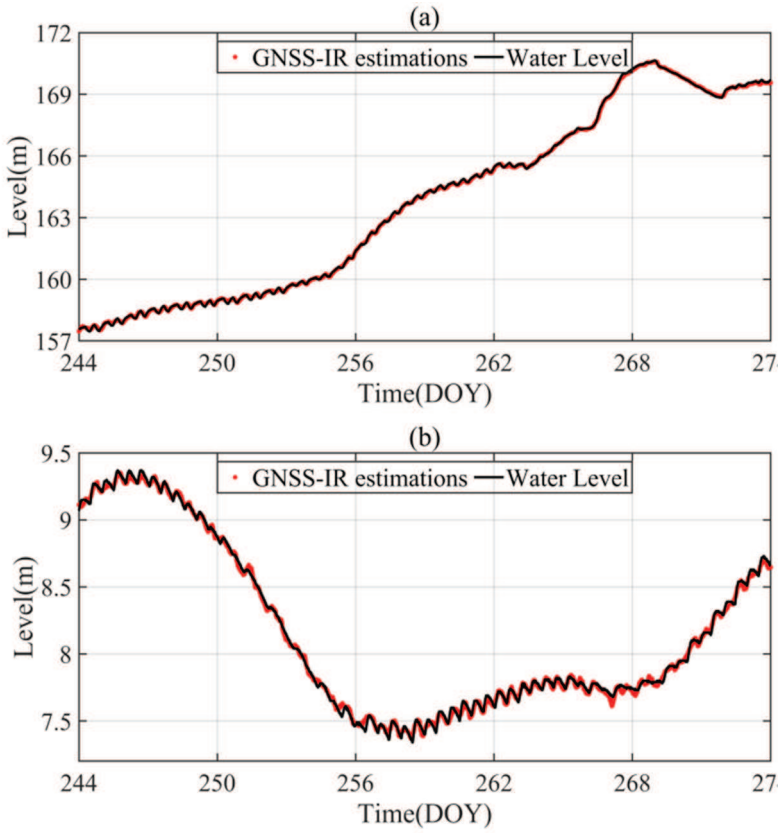

Fig. 8. Comparison of GNSS-IR combination algorithm retrieval results with water level gauge measurements. (a) BADO and (b) DATO.

results indicate that VMD offers advantages in accuracy, data utilization efficiency, and temporal resolution, making it a reliable choice for high-frequency water level monitoring.

We used the IRLS method to merge retrieval results from VMD and LSP and then refined the final output with S–G filters. During the test period, the water gauge recorded 8640 observations. The BADO and DATO stations generated 8057 and 8475 retrieval results, respectively, with void retrievals accounting for 6.7% and 1.9% of the total results. Void retrievals occur when there are no transit satellites in the window or when no usable reflector height is available after quality control. To address these voids in GNSS-IR data, this article applies cubic spline interpolation.

Fig. 7 shows the number of valid retrievals and the corresponding number of windows during the combination algorithm process. In BADO, 24.28% of the windows had three valid retrievals, with most windows showing between one and five valid retrievals. In contrast, DATO had an average of five valid retrievals per window, resulting in a significantly higher total number of retrievals compared to BADO.

Fig. 8 displays the comparison between the GNSS-IR combined algorithm results and the water level gauge

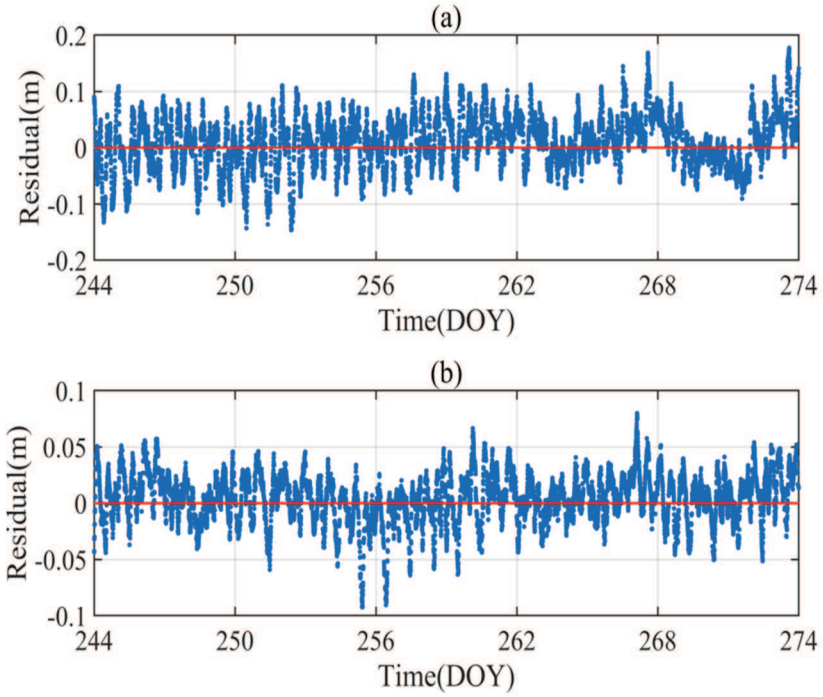

Fig. 9. Residuals between GNSS-IR combination algorithm water level inversion results and water level gauge measurements for (a) BADO and (b) DATO.

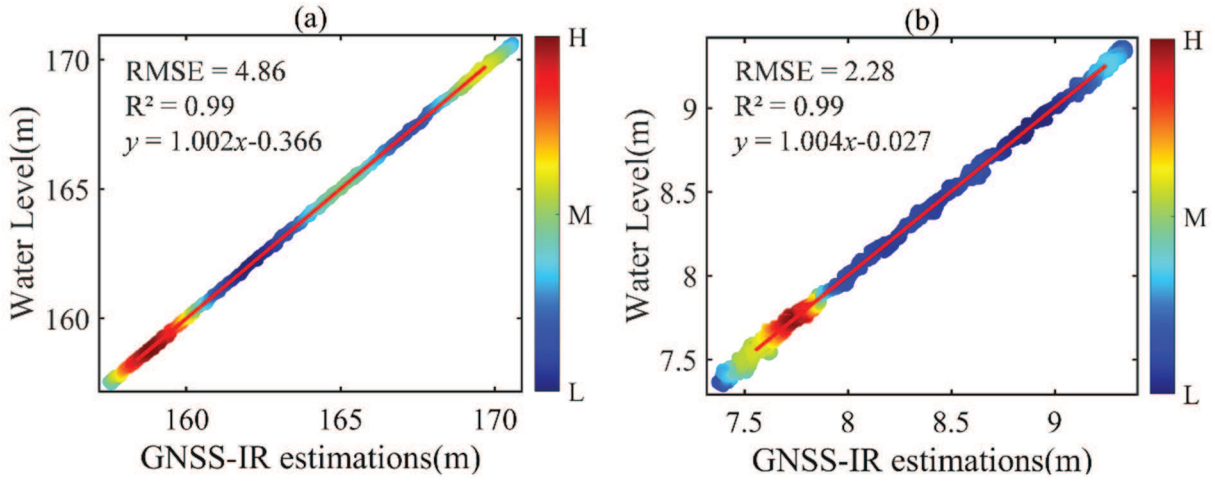

Fig. 10. Correlation analysis charts between water level gauge measurements and GNSS-IR combined algorithm results for (a) BADO and (b) DATO.

measurements. During the test period, the water level at BADO fluctuated significantly with a maximum drop of 13 m. The GNSS-IR estimates (red dots) show high consistency with the water gauge measurements (black line), with overall deviations within ±0.2 m (Fig. 9). The water level fluctuations at DATO were relatively minimal (Fig. 8), which provides a detailed comparison between the GNSS-IR estimates and water gauge measurements. Notably, there was a significant deviation during a trough on DOY 267, but the overall deviation remained within ±0.1 m (Fig. 9). In addition, the correlation analysis, shown in Fig. 10, reveals that the RMSE for BADO and DATO are 4.86 and 2.28 cm, respectively, with both R^2 over 0.99. This indicates that the GNSS-IR combination algorithm effectively captures water level changes, whether the water level is steadily rising or fluctuating slightly.

IV. Discussion

In this study, we utilized a combined GNSS algorithm to retrieve water level data for the river with a temporal resolution of 5 min (DOY 244–273) along the Yangtze River. The results show that, compared to water gauges, the RMSE at the two stations (BADO and DATO) were 4.86 and 2.28 cm, respectively. Accuracy improved by at least 45.88% and 67.52% compared to individual signal results, with both stations achieving R^2 of 0.99. Moreover, most residuals at both stations were within ±0.1 m, demonstrating that this method effectively captures water level changes, whether during steady increases or minor fluctuations. In the combined approach, the VMD method effectively filters out direct signals and noise, enhancing the accuracy of spectral analysis compared to other methods. The IRLS method successfully integrates estimates

from multiple GNSS systems, improving the overall accuracy and stability of water level retrieval results. The application of the SG smoothing filter to the combined results further refined the estimates, reducing noise and smoothing short-term fluctuations, resulting in smoother and more continuous water level estimation curves.

This study demonstrates that the combined method is effective for high-frequency water level monitoring using GNSS-IR technology along the Yangtze River. Although there are slight differences in water level estimation accuracy between the BADO and DATO stations, these variations are due to two main factors: the differing trends in water level changes between the upstream and downstream sections of the Yangtze River and the differences in the number of observable satellites. BADO is located upstream of the Three Gorges Dam and is directly influenced by dam operations and upstream water inflows. This results in more complex and larger fluctuations in water levels. The amplitude of water level fluctuations in this environment may be higher, with more frequent changes in reflected signals, which increases the complexity and difficulty of water level estimation. In contrast, the downstream DATO station, influenced by multiple reservoir management practices, experiences relatively stable water level changes. This results in smaller fluctuations and more stable reflected signals. In addition, differences in the number of observable satellites may contribute to variations in accuracy. Specifically, the BADO station has fewer band retrieval results compared to DATO, particularly with less contribution from the Galileo system. This implies that the robustness of the BADO station is relatively weaker in the multisystem combination process.

This study has some limitations. For example, as reflected signals pass through the troposphere, refraction causes the signal path to bend, leading to an increased elevation angle [39]. This study did not correct for the effects of tropospheric delay, which may introduce some level of error. Future studies could improve water level estimation accuracy by incorporating tropospheric correction for reflected signals.

V. Conclusion

The high-frequency and high-accuracy water level is estimated in real time at the Yangtze River stations (BADO and DATO) based on a combined method utilizing reflected signals from GPS, GLONASS, Galileo, and BDS constellations. The study demonstrates the effectiveness of the proposed GNSS-IR combined method for high-frequency and high-accuracy water level monitoring. By combining the sliding window with VMD, IRLS, and S–G filtering, centimeter-level accuracy and 5-min time resolution water levels are achieved. The results show that VMD outperforms other methods, such as QF, EMD, and SSA, in terms of accuracy and data utilization efficiency. Although the performance of the BADO and DATO stations varies slightly, this can be attributed to differences in water level dynamics between the river's upstream and downstream sections, as well as variations in the number of observable satellites, particularly the contribution from the Galileo system.

Overall, GNSS-IR is a reliable and valuable tool for continuously and accurately monitoring water levels. This provides a strong basis for the broader application of GNSS-IR technology in hydrological monitoring and water resource management. As the technology advances, it is expected to play a crucial role in tackling challenges associated with water management and environmental sustainability in the future [40], [41].

Acknowledgment

The authors are grateful to the reviewers for their constructive feedback and insightful comments on this article.

References

[1] G. Feng, S. Jin, and T. Zhang, "Coastal sea level changes in Europe from GPS, tide gauge, satellite altimetry and GRACE, 1993–2011," *Adv. Space Res.*, vol. 51, no. 6, pp. 1019–1028, Mar. 2013.

[2] S. Jin et al., "Remote sensing and its applications using GNSS reflected signals: Advances and prospects," *Satell. Navigat.*, vol. 5, no. 1, p. 19, May 2024.

[3] C. D. Hall and R. A. Cordey, "Multistatic scatterometry," in *Proc. Int. Geosci. Remote Sens. Symp., Remote Sens., Moving Toward 21st Century*, Sep. 1988, pp. 561–562.

[4] H. Qiu and S. Jin, "Global mean sea surface height estimated from spaceborne cyclone-GNSS reflectometry," *Remote Sens.*, vol. 12, no. 3, p. 356, Jan. 2020.

[5] M. Ma, S. Jin, and X. T. Jin, "Characteristics of ionospheric disturbances during the 2021 typhoon chanthu based on GPS and GLONASS," *Adv. Space Res.*, vol. 74, no. 1, pp. 271–283, Jul. 2024.

[6] A. Regmi, M. E. Leinonen, A. Pärssinen, and M. Berg, "Monitoring sea ice thickness using GNSS-interferometric reflectometry," *IEEE Geosci. Remote Sens. Lett.*, vol. 19, pp. 1–5, 2022.

[7] A. Calabia, I. Molina, and S. Jin, "Soil moisture content from GNSS reflectometry using dielectric permittivity from Fresnel reflection coefficients," *Remote Sens.*, vol. 12, no. 1, p. 122, Jan. 2020.

[8] Y. Hu, X. Yuan, W. Liu, J. Wickert, and Z. Jiang, "GNSS-R snow depth inversion based on variational mode decomposition with multi-GNSS constellations," *IEEE Trans. Geosci. Remote Sens.*, vol. 60, 2022, Art. no. 2005512.

[9] M. Martin-Neira, "A passive reflectometry and interferometry system (PARIS): Application to ocean altimetry," *ESA J.*, vol. 17, no. 4, pp. 331–355, 1993.

[10] K. D. Anderson, "Determination of water level and tides using interferometric observations of GPS signals," *J. Atmos. Ocean. Technol.*, vol. 17, no. 8, pp. 1118–1127, Aug. 2000.

[11] A. Santamaría-Gómez, C. Watson, M. Gravelle, M. King, and G. Wöppelmann, "Levelling co-located GNSS and tide gauge stations using GNSS reflectometry," *J. Geodesy*, vol. 89, no. 3, pp. 241–258, Mar. 2015.

[12] J. C. Kucwaj, G. Stienne, S. Reboul, J.-B. Choquel, and M. Benjelloun, "Accurate pseudorange estimation by means of code and phase delay integration: Application to GNSS-R altimetry," *IEEE J. Sel. Topics Appl. Earth Observ. Remote Sens.*, vol. 9, no. 10, pp. 4854–4864, Oct. 2016.

[13] K. M. Larson, J. S. Löfgren, and R. Haas, "Coastal sea level measurements using a single geodetic GPS receiver," *Adv. Space Res.*, vol. 51, no. 8, pp. 1301–1310, Apr. 2013.

[14] K. M. Larson, R. D. Ray, F. G. Nievinski, and J. T. Freymueller, "The accidental tide gauge: A GPS reflection case study from Kachemak Bay, Alaska," *IEEE Geosci. Remote Sens. Lett.*, vol. 10, no. 5, pp. 1200–1204, Sep. 2013.

[15] J. S. Löfgren and R. Haas, "Sea level measurements using multi-frequency GPS and GLONASS observations," *EURASIP J. Adv. Signal Process.*, vol. 2014, no. 1, pp. 1–13, Dec. 2014.

[16] S. Jin, X. Qian, and X. Wu, "Sea level change from BeiDou navigation satellite system-reflectometry (BDS-R): First results and evaluation," *Global Planet. Change*, vol. 149, pp. 20–25, Feb. 2017.

[17] N. Roussel et al., "Sea level monitoring and sea state estimate using a single geodetic receiver," *Remote Sens. Environ.*, vol. 171, pp. 261–277, Dec. 2015.

[18] X. Wang, X. He, and Q. Zhang, "Evaluation and combination of quad-constellation multi-GNSS multipath reflectometry applied to sea level retrieval," *Remote Sens. Environ.*, vol. 231, Sep. 2019, Art. no. 111229.

[19] J. Strandberg, T. Hobiger, and R. Haas, "Improving GNSS-R sea level determination through inverse modeling of SNR data," *Radio Sci.*, vol. 51, no. 8, pp. 1286–1296, Aug. 2016.

[20] J. Strandberg, T. Hobiger, and R. Haas, "Real-time sea-level monitoring using Kalman filtering of GNSS-R data," *GPS Solutions*, vol. 23, no. 3, Jul. 2019, Art. no. 61.
[21] J. Beckheinrich, A. Hirrle, S. Schön, G. Beyerle, M. Semmling, and J. Wickert, "Water level monitoring of the Mekong delta using GNSS reflectometry technique," in *Proc. IGARSS*, Jul. 2014, pp. 3798–3801.
[22] C. B. Lee, C. Fu, W. Lan, and C. Kuo, "Performance evaluation of different reflected signal extraction methods on GNSS-R derived sea level heights," *Adv. Space Res.*, vol. 74, no. 1, pp. 89–104, Jul. 2024.
[23] P. L. Vu et al., "Identifying 2010 xynthia storm signature in GNSS-R-based tide records," *Remote Sens.*, vol. 11, no. 7, p. 782, Apr. 2019.
[24] M. Raiabi et al., "A performance assessment of polarimetric GNSS-R sea level monitoring in the presence of sea surface roughness," in *Proc. IEEE Int. Geosci. Remote Sens. Symp. (IGARSS)*, Jul. 2021, pp. 8328–8331.
[25] Y. Hu, X. Yuan, W. Liu, J. Wickert, Z. Jiang, and R. Haas, "GNSS-IR model of sea level height estimation combining variational mode decomposition," *IEEE J. Sel. Topics Appl. Earth Observ. Remote Sens.*, vol. 14, pp. 10405–10414, 2021.
[26] Z. Chen and S. Jin, "High-frequency water level estimation in the Yangtze river from GNSS-interferometric reflectometry," in *Proc. Photon. Electromagn. Res. Symp. (PIERS)*, Apr. 2024, pp. 1–5.
[27] F. Geremia-Nievinski and K. M. Larson, "Forward modeling of GPS multipath for near-surface reflectometry and positioning applications," *GPS Solutions*, vol. 18, no. 2, pp. 309–322, Apr. 2013.
[28] A. Bilich and K. M. Larson, "Correction published 29 March 2008: Mapping the GPS multipath environment using the signal-to-noise ratio (SNR)," *Radio Sci.*, vol. 42, no. 6, pp. 1–16, Dec. 2007.
[29] N. R. Lomb, "Least-squares frequency analysis of unequally spaced data," *Astrophys. Space Sci.*, vol. 39, no. 2, pp. 447–462, Feb. 1976.
[30] J. D. Scargle, "Studies in astronomical time series analysis. II—Statistical aspects of spectral analysis of unevenly spaced data," *Astrophys. J.*, vol. 1, pp. 835–853, Dec. 1982.
[31] S. Jin, Q. Wang, and G. Dardanelli, "A review on multi-GNSS for Earth observation and emerging applications," *Remote Sens.*, vol. 14, no. 16, p. 3930, Aug. 2022.
[32] M. Ye, S. Jin, and Y. Jia, "Ten-minute sea-level variations from combined multi-GNSS multipath reflectometry based on a weighted iterative least-square method," *IEEE Trans. Geosci. Remote Sens.*, vol. 60, 2022, Art. no. 4208510.
[33] K. Dragomiretskiy and D. Zosso, "Variational mode decomposition," *IEEE Trans. Signal Process.*, vol. 62, no. 3, pp. 531–544, Feb. 2014.
[34] W. Wu, Z. Wang, J. Zhang, W. Ma, and J. Wang, "Research of the method of determining k value in VMD based on kurtosis," *J. Mech. Transmiss.*, vol. 42, no. 8, pp. 153–157, 2018.
[35] Z. Liu, L. Du, P. Zhou, X. Wang, Z. Zhang, and Z. Liu, "Cloud-based near real-time sea level monitoring using GNSS reflectometry," *GPS Solutions*, vol. 27, no. 2, p. 65, Feb. 2023.
[36] Y. Yuanxi, "Robust estimation for dependent observations," *Manuscripta Geodaetica*, vol. 19, no. 1, pp. 10–17, Feb. 1994.
[37] P. A. Gorry, "General least-squares smoothing and differentiation by the convolution (Savitzky-Golay) method," *Anal. Chem.*, vol. 62, no. 6, pp. 570–573, Mar. 1990.
[38] C. Altuntas and N. Tunalioglu, "GIRAS: An open-source MATLAB-based software for GNSS-IR analysis," *GPS Solutions*, vol. 26, no. 1, Nov. 2021, Art. no. 16.
[39] S. Williams and F. Geremia-Nievinski, "Tropospheric delays in ground-based GNSS multipath reflectometry—Experimental evidence from coastal sites," *J. Geophys. Res. Solid Earth*, vol. 122, no. 3, pp. 2310–2327, Mar. 2017.
[40] S. G. Jin, X. Wu, and H. Qiu, *GNSS-Reflectometry: Fundamentals, Methods and Applications*. Berlin, Germany: Springer, May 2025.
[41] S. Jin, X. Meng, G. Dardanelli, and Y. Zhu, "Multi-global navigation satellite system for Earth observation: Recent developments and new progress," *Remote Sens.*, vol. 16, no. 24, p. 4800, Dec. 2024.

Shuanggen Jin (Senior Member, IEEE) was born in Anhui, China, in September 1974. He received the B.Sc. degree in geodesy from Wuhan University, Wuhan, China, in 1999, and the Ph.D. degree in geodesy from the University of Chinese Academy of Sciences, Beijing, China, in 2003.

He is currently the Vice-President and a Professor at Henan Polytechnic University, Jiaozuo, China. He has published over 500 article in peer-reviewed journals and proceedings, 30 patents/software copyrights, three codes and standards, and 15 books/monographs with more than 17 000 citations and H-index of 70. His main research areas include satellite navigation, remote sensing, and space/planetary exploration.

Prof. Jin was an IUGG Fellow, an IETI Fellow, an IAG Fellow, an AAIS Fellow, an EMA Fellow, the World Class Professor of Ministry of Education and Cultures, Indonesia, the Chief Scientist of the National Key Research and Development Program, China, a member of European Academy of Sciences, a member of Turkish Academy of Sciences, and a member of Academia Europaea. He received 100-Talent Program of CAS. He was the President of International Association of Planetary Sciences (IAPS) from 2015 to 2019, the President of the International Association of Chinese Professionals in GNSS (CPGNSS) from 2016 to 2017, the Chair of IUGG Union Commission on Planetary Sciences (UCPS) from 2015 to 2027, the Editor-in-Chief of *International Journal of Geosciences*, an Associate Editor of IEEE TRANSACTIONS ON GEOSCIENCE AND REMOTE SENSING and *Journal of Navigation*, and an Editorial Board Member of *GPS Solutions* and *Journal of Geodynamics*.

Zilong Chen received the master's degree in geomatics engineering from Nanjing University of Information Science and Technology, Nanjing, China.

His research interests include global navigation satellite system (GNSS) remote sensing and its applications.

Hui Peng (Member, IEEE) received the master's degree in geomatics engineering from Nanjing University of Information Science and Technology, Nanjing, China.

His research interests include global navigation satellite system (GNSS) ionospheric modeling and its applications.